Low Electronic Conductivity of $Li_7La_3Zr_2O_{12}$ (LLZO) Solid Electrolytes from First Principles

Alexander G. Squires,[†,§] Daniel W. Davies,[‡] Sunghyun Kim,[¶] David O. Scanlon,[‡,§] Aron Walsh,[¶,§] and Benjamin J. Morgan[*,†,§]

†*Department of Chemistry, University of Bath, Claverton Down BA2 7AY, United Kingdom*
‡*Department of Chemistry, University College London, 20 Gordon Street, London, WC1H 0AJ.*
¶*Department of Materials, Imperial College London, Exhibition Road, London SW7 2AZ, United Kingdom*
§*The Faraday Institution, Quad One, Becquerel Avenue, Harwell Campus, Didcot, OX11 0RA, United Kingdom*
‖*Diamond Light Source Ltd., Diamond House, Harwell Science and Innovation Campus, Didcot, Oxfordshire OX11 0DE, United Kingdom.*
⊥*Department of Materials Science and Engineering, Yonsei University, Seoul 03722, Korea*

E-mail: b.j.morgan@bath.ac.uk

Abstract

Lithium-rich garnets such as $Li_7La_3Zr_2O_{12}$ (LLZO) are promising solid electrolytes with potential applications in all–solid-state lithium-ion batteries. The practical use of lithium-garnet electrolytes is currently limited by pervasive lithium-dendrite growth during battery cycling, which leads to short-circuiting and cell failure. One proposed mechanism for dendrite growth is the reduction of lithium ions to lithium metal within the electrolyte. Lithium garnets have been proposed to be susceptible to this growth mechanism due to high electronic conductivities [Han *et al. Nature Ener.* **4** 187, 2019]. The electronic conductivities of LLZO and other lithium-garnet solid electrolytes, however, are not yet well characterised. Here, we present a general scheme for calculating the intrinsic electronic conductivity of a nominally-insulating material under variable synthesis and operating conditions from first principles, and apply this to the prototypical lithium-garnet LLZO. Our model predicts that under typical battery operating conditions, electron and hole carrier-concentrations in bulk LLZO are negligible, irrespective of initial synthesis conditions, and electron and hole mobilities are low ($<1\,cm^2\,V^{-1}\,s^{-1}$). These results suggest that the bulk electronic conductivity of LLZO is not sufficiently high to cause bulk lithium-dendrite formation during cell operation. Any non-negligible electronic conductivity in lithium garnets is therefore likely due to extended defects or surface contributions.

The ongoing global transition to a low-carbon economy is dependent on significant future advances in electrochemical energy-storage technologies. A key area of research is the replacement of the graphitic intercalation anodes used in conventional lithium-ion batteries with lithium-metal anodes, which allow greatly increased cell energy-densities.[1–3] The development of practical lithium-metal batteries, however, is impeded by pervasive lithium-dendrite growth during cycling. Dendrites typically nucleate at structural or electrical inhomogeneities at the anode–electrolyte interface and then grow towards the cathode, ultimately creating an electrical contact that causes the battery to fail by short circuit.[1,4]

One strategy to supress dendrite propagation in lithium-metal–anode cells is to replace the conventional liquid electrolytes used in commercial cells with a solid lithium-ion–conducting ceramic, with the expectation that a solid electrolyte should have sufficient mechanical hardness to block dendrite growth.[5,6] To this end, a number of solid lithium-ion electrolytes have been developed, with some demonstrating ionic conductivities comparable to those of conventional liquid electrolytes.[7–11] The lithium-stuffed garnets, such as $Li_7La_3Zr_2O_{12}$ (LLZO), have gained particular interest due to their dual properties of high room-temperature lithium-ion conductivities ($\sim 1\,mS\,cm^{-1}$)[12] and wide electrochemical-stability windows, which are required for a stable interface with lithium metal.[13]

Despite the promise of all–solid-state batteries based on lithium-garnet solid electrolytes, garnet-electrolyte–lithium-metal cells still exhibit lithium-dendrite growth and associated short-circuiting. Understanding the causal mechanism for this process is a key research question, because this may suggest a strategy for suppressing dendrite growth in lithium-garnets and related solid electrolytes.[14–21] One proposed mechanism for dendrite-formation is that mobile electrons in the solid electrolyte can directly reduce lithium ions to lithium metal,[15,22] and these internal metallic deposits then

grow to form dendrites.[1] This proposed mechanism of "bulk" lithium reduction due to intrinsic bulk electronic conductivity suggests that to limit dendrite growth in lithium-ion solid electrolytes it is neccessary not only to control surface and interface features—for example, limiting surface defects that might act as nucleation sites—but also to target solid electrolytes with sufficiently low electronic conductivities to suppress bulk dendrite-nucleation. On this basis, Han *et al.* have proposed empirical upper limits for desirable electronic conductivities in lithium-ion solid electrolytes for dendrite-free lithium plating of $10^{-10}\,\mathrm{S\,cm^{-1}}$ and $10^{-12}\,\mathrm{S\,cm^{-1}}$ at current densities of $1\,\mathrm{mA\,cm^{-2}}$ and $10\,\mathrm{mA\,cm^{-2}}$, respectively.[15]

The factors that dictate the electronic conductivities of specific solid electrolytes are, in general, not well understood. Lithium-ion solid electrolytes usually possess wide band-gaps and low-curvature valence- and conduction-band edges,[13] suggesting low intrinsic electronic conductivities consistent with their typical characterisation as electronic insulators. Consequently, non-negligible electronic conductivities observed in experimental samples are usually attributed to contributions from grain boundaries or surface effects.[18,19] The threshold electronic conductivities proposed by Han *et al.* are very low, however,[2] and it is possible that in solid electrolytes such as the lithium garnets the presence of point defects introduces sufficient numbers of electronic carriers that the bulk electronic conductivities can exceed these threshold values.[15]

Motivated by these considerations, we have performed a first-principles computational study of the bulk electronic conductivity of the prototypical lithium-garnet solid electrolyte $Li_7La_3Zr_2O_{12}$ (LLZO). We present a computational workflow for: 1. Calculating electron and hole carrier concentrations across a range of synthesis and operating conditions and under varied doping regimes, and 2. Calculating electron and hole mobilities. Combining these quantities gives a fully first-principles prediction of the electronic conductivity as a function of synthesis protocol, i.e. synthesis conditions plus dopant concentrations.

Theory

The electronic conductivity, σ, of a semiconductor is given by

$$\sigma = n_0 q \mu_\mathrm{n} + p_0 q \mu_\mathrm{p}, \tag{1}$$

where n_0 and p_0 are the concentrations of free electrons and holes respectively, q is the magnitude of charge of each carrier species, and μ_n and μ_p are the electron and hole mobilities. For wide-gap materials, such as solid electrolytes, the thermal energy at room-temperature is insufficient to generate free carriers by directly exciting electrons from the valence band to the conduction band. The presence of point defects, however, can produce free charge carriers.[26,27] Point defects exist even in nominally stoichiometric samples due to configurational entropy, or may be introduced by deliberate (or inadvertent) doping with extrinsic species.[28–30] Aliovalent doping of solid electrolytes is a common synthesis strategy to increase ionic conductivities through modulation of the number of ionic charge carriers.[31–33] A secondary effect of aliovalent doping, however, is to shift the position of the Fermi energy within the band gap. Moving the Fermi energy closer to either the conduction-band or valence-band edges increases the number of thermally generated electrons or holes (respectively). Under select synthesis conditions and doping protocols, therefore, the Fermi energy can move close enough to either the valence- or conduction-band edge that the population of thermally generated electronic charge carriers is sufficiently high to give a non-negligible electronic conductivity.

Electron and hole carrier concentrations can be calculated as functions of the Fermi energy, E_F, and the bulk electronic density of states, $g(E)$;

$$n_0 = \int_0^\infty \frac{1}{\mathrm{e}^{(E-E_\mathrm{F})/k_\mathrm{B}T}+1} g(E)\,\mathrm{d}E, \tag{2}$$

$$p_0 = \int_0^\infty 1 - \frac{1}{\mathrm{e}^{(E-E_\mathrm{F})/k_\mathrm{B}T}+1} g(E)\,\mathrm{d}E, \tag{3}$$

where k_B is the Boltzmann constant.[34] Point defect concentrations are given by

$$[X^q] = N_0^X \exp\left(\frac{\Delta E_\mathrm{f}^{X,q}[E_\mathrm{F}, \Delta\mu_i]}{k_\mathrm{B}T}\right), \tag{4}$$

where N_0^X is the density of available sites for defect X, $\Delta E_\mathrm{f}^{X,q}$ is the formation energy of defect X in charge-state q, which in turn depends on the Fermi energy, E_F, and $\Delta\mu_i$ are the chemical potentials of any atomic species added to or removed from the system when forming each defect.[35,36] Equations 2, 3, and 4 are coupled by a common Fermi energy, which itself is constrained by the requirement that the system is net charge-neutral—the charge-density contributions from electrons, holes, and any charged point-defects must sum to zero;

$$\rho(E_\mathrm{F}) = \sum_{X^q} q[X^q] + p_0 - n_0 = 0. \tag{5}$$

Calculating equilibrium carrier concentrations under specific synthesis conditions—which define the external chemical potentials—consists of finding a self-consistent solution to Equations 2, 3, and 4, subject to the charge-neutrality constraint expressed in Equation 5.[35,37]

[1] An analogous degradation process due to reduction of Na^+ to Na^0 resulting from electronic conduction has been discussed for Na-beta-alumina.[23,24]

[2] For comparison, the conductivity of the commercial transparent conducting oxide Sn-doped In_2O_3 is on the order of $10^3\,\mathrm{S/cm}$[25]—$\times 10^{13}$ larger than the upper threshold proposed by Han *et al.*

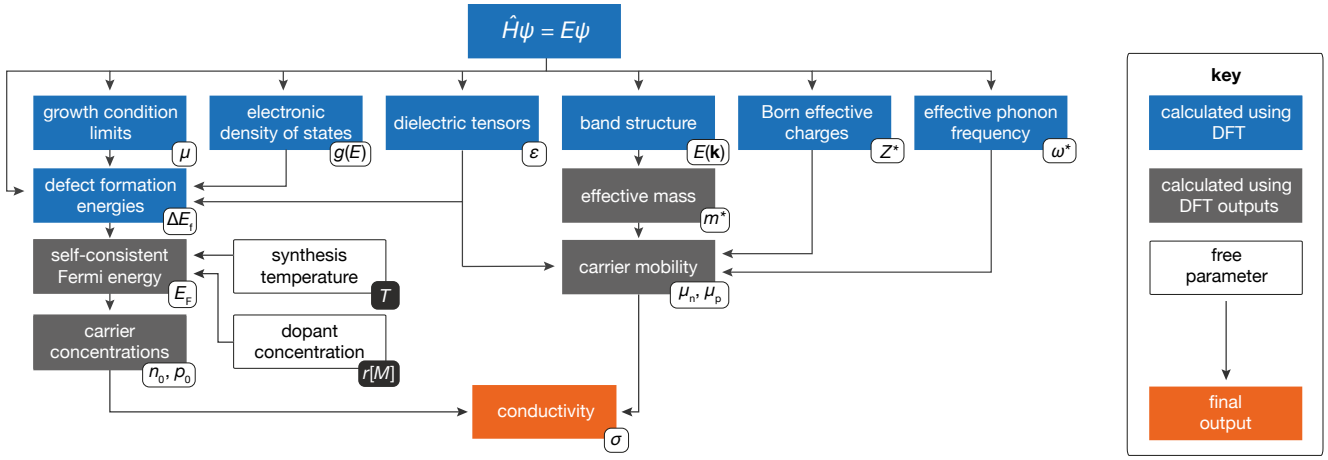

Figure 1: Schematic showing the workflow used to calculate the electronic conductivity from first-principles inputs.

The effect of extrinsic dopants can be accounted for by including an additional term in Equation 5.[28,30,37] For a dopant M with relative charge r and fixed concentration $[M^r]$, ρ becomes

$$\rho(E_\mathrm{F}, r[M^r]) = \sum_{X^q} q[X^q] + p_0 - n_0 + r[M^r]. \qquad (6)$$

In the dilute-defect–limit there is no direct interaction between dopants and native defects, and the doping response does not depend explicitly on the choice of dopant species and insertion site but only on the product $r[M^r]$.

The necessary inputs to solve Equations 2—6 are the reference elemental chemical potentials, which are restricted by the condition that the host material being considered must be thermodynamically stable with respect to likely degradation products; the native defect formation energies; the dielectric tensor for the material, which is used to correct for spurious implicit interactions between defects and their periodic images during formation energy calculations;[38] and the electronic density of states for the non-defective system. These parameters can all be obtained using first-principles methods such as Density Functional Theory (DFT).[39,40] The mobilities of the electron and hole charge carriers—μ_n and μ_p, respectively—can be calculated using the Feynman variational solution for Fröhlich's polaron Hamiltonian and integrating the polaron-response function to obtain a mobility.[41,42] This method for calculating polaron mobilities assumes that charge-carrier mobilities are limited by scattering by optical phonon modes, which dominates for heteropolar crystals.[43] The inputs for this calculation are the dielectric constant of the solid electrolyte, Born effective charges, a characteristic phonon frequency and charge-carrier effective masses: again, these are all calculable using first-principles methods.[44]

We now turn to the application of this theoretical framework, illustrated schematically in Fig. 1, to calculate the electronic conductivity of LLZO. All calculations were performed on the low-temperature tetragonal phase of LLZO, as opposed to the high–ionic-conductivity high-temperature cubic phase. A key component of our model is the accurate calculation of self-consistent point-defect populations. The high-temperature cubic phase of LLZO has highly mobile lithium ions and high intrinsic lithium disorder. This violates the assumptions used in the derivation of Eqn. 4, which is formally valid only for systems with an ordered ground-state.[28] Rather than introduce unquantified errors—by assuming Eqn. 4 holds for an inherently disordered system—we instead consider the low-temperature lithium-ordered LLZO phase and assume that the close structural similarity between the ordered and disordered LLZO phases—excepting the degree of lithium disorder—means our results provide at least an order-of-magnitude estimate of the electronic conductivity in practical lithium-garnet solid electrolytes.

Results

Carrier Mobilities. The electronic conductivity is given by the products of carrier concentrations and carrier mobilities, summed over contributions from both electron and hole carriers (Eqn. 1). For the carrier mobilities, we are interested in these values under typical cell operating conditions, which we take as 298 K. Our model assumes that the carrier mobilities do not vary with changes in synthesis conditions or doping levels. The carrier mobilities therefore act as fixed scaling factors that can be used to convert carrier concentrations—which do vary according to synthesis conditions and doping levels—into electronic conductivities.

To calculate carrier mobilities, we first determine the electron and hole effective masses. Carrier populations in wide-gap insulators such as LLZO are low compared to conventional semiconductors, and we therefore calculate *curvature* effective-masses at the conduction band minimum (CBM) and valence band maximum (VBM).[45] The band-structure for t-LLZO is shown in Fig. 2, and the resulting curvature effective masses are

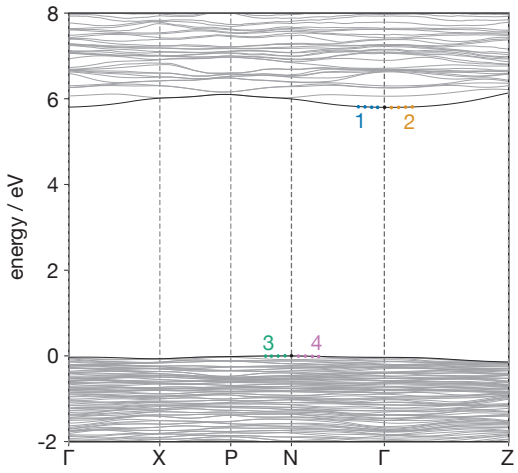

Figure 2: The electronic band structure of t-LLZO calculated using HSE06, plotted along a high symmetry path in the Brillouin zone according to the Bradley and Cracknell notation.[46] The coloured points mark the band edges used to calculate the effective masses, with numeric labels indicating the corresponding entry in Table 1.

given in Table 1. Additional inputs for solving Fröhlich's polaron Hamiltonian include dielectric constants, calculated as $\epsilon_{\text{ion}} = 23.12$, and $\epsilon_{\infty} = 2.07$. This large discrepancy between ionic (ϵ_{ion}) and high frequency ($\epsilon_{\infty} = 2.07$) dielectric response implies large electron–phonon coupling.[44] Using these data to calculate maximum room-temperature carrier mobility (considering both at the VBM and CBM) yields a value of of $0.06\,\text{cm}^2\,\text{V}^{-1}\,\text{s}^{-1}$.

Table 1: Curvature effective masses, m^*, for holes and electrons determined by a parabolic fit to LLZO band edges,[47] and the relevant crystallographic direction for transport. Numbers indicate the corresponding features in the electronic band structure (Fig. 2).

Carrier	Direction	m^*	No.
electron	$\Gamma \longrightarrow$ N	2.35	1
electron	$\Gamma \longrightarrow$ Z	2.41	2
hole	N $\longrightarrow$ P	2.39	3
hole	N $\longrightarrow \Gamma$	21.44	4

Carrier Concentrations. The electron and hole carrier populations are given by Eqns. 2 and 3, which are solved self-consistently along with Eqn. 4 (which describes point-defect concentrations) under the constraint of net charge-neutrality (Eqns. 5 or 6). This self-consistent calculation requires specifying the thermodynamic conditions, i.e. defining the temperature, which appears in Eqns. 2, 4; and the reference elemental chemical potentials, which affect the defect formation energies via Eqn. 4. While our model treats the elemental chemical potentials as free parameters, in our analysis we restrict this chemical potential space

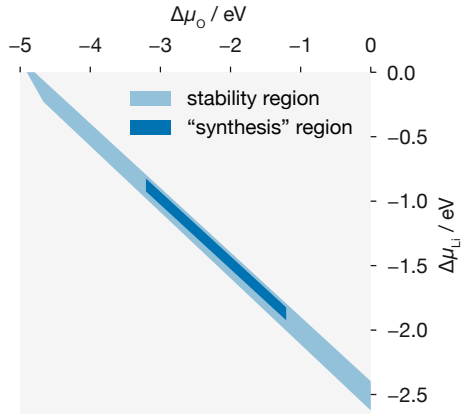

Figure 3: Chemical potential stability region of LLZO in the $\{\Delta\mu_{\text{Li}}, \Delta\mu_{\text{O}}\}$ plane. The dark blue region is constricted by Equation 7 to represent synthesis conditions ranging from $T = 1000\,\text{K}$ to $1500\,\text{K}$ and $P_{\text{O}_2} = 1\,\text{atm}$ to $1 \times 10^{-10}\,\text{atm}$.

to values that are, in principle, experimentally accessible; we consider only sets of chemical potentials for which LLZO is thermodynamically stable with respect to competing phases. For this stability analysis, we have considered the set of competing phases identified by Canepa *et al.*[48] The predicted region of thermodynamic stability of LLZO spans a range of values in four-dimensional $\{\Delta\mu_{\text{Li}}, \Delta\mu_{\text{O}}, \Delta\mu_{\text{La}}, \Delta\mu_{\text{Zr}}\}$ chemical-potential space that can be broadly characterised along an O-rich/metal-poor→O-poor/metal-rich axis. To further restrict this region to values corresponding to typical synthesis conditions, we relate the oxygen chemical potential to the synthesis pressure, P, and temperature, T, via

$$\Delta\mu_{\text{O}}(T,P) = \frac{1}{2}\left\{(T - T_0) - T\left[S_0 + C_p \ln\frac{T}{T_0} + k_{\text{B}} \ln\frac{P}{P_0}\right]\right\}, \tag{7}$$

using the experimental value for the oxygen standard entropy, $S_0 = 205\,\text{J}\,\text{mol}^{-1}\,\text{K}^{-1}$.[49] Assuming oxygen behaves as an ideal gas, we use $C_p = (7/2)\ k_{\text{B}}$ for the constant-pressure specific–heat-capacity per diatomic molecule. This reproduces well experimentally tabulated values of $\Delta\mu_{\text{O}}(T,P)$, with a maximum error of ∼15 meV at the higher end of the temperature range under which LLZO is typically synthesised (1500 K).[50,51] The full thermodynamic-stability region of LLZO is limited by the additional constraints we place on the oxygen chemical potential, corresponding to synthesis temperatures of 1000 K to 1500 K, and oxygen partial pressures of 1 atm to 1×10^{-10} atm. The reduced synthetically accessible chemical potential volume is plotted in the $\{\Delta\mu_{\text{Li}}, \Delta\mu_{\text{O}}\}$ plane in Fig. 3.

While LLZO is typically synthesised at high temperature (up to 1500 K), we are ultimately interested in predicting the electronic conductivity at much

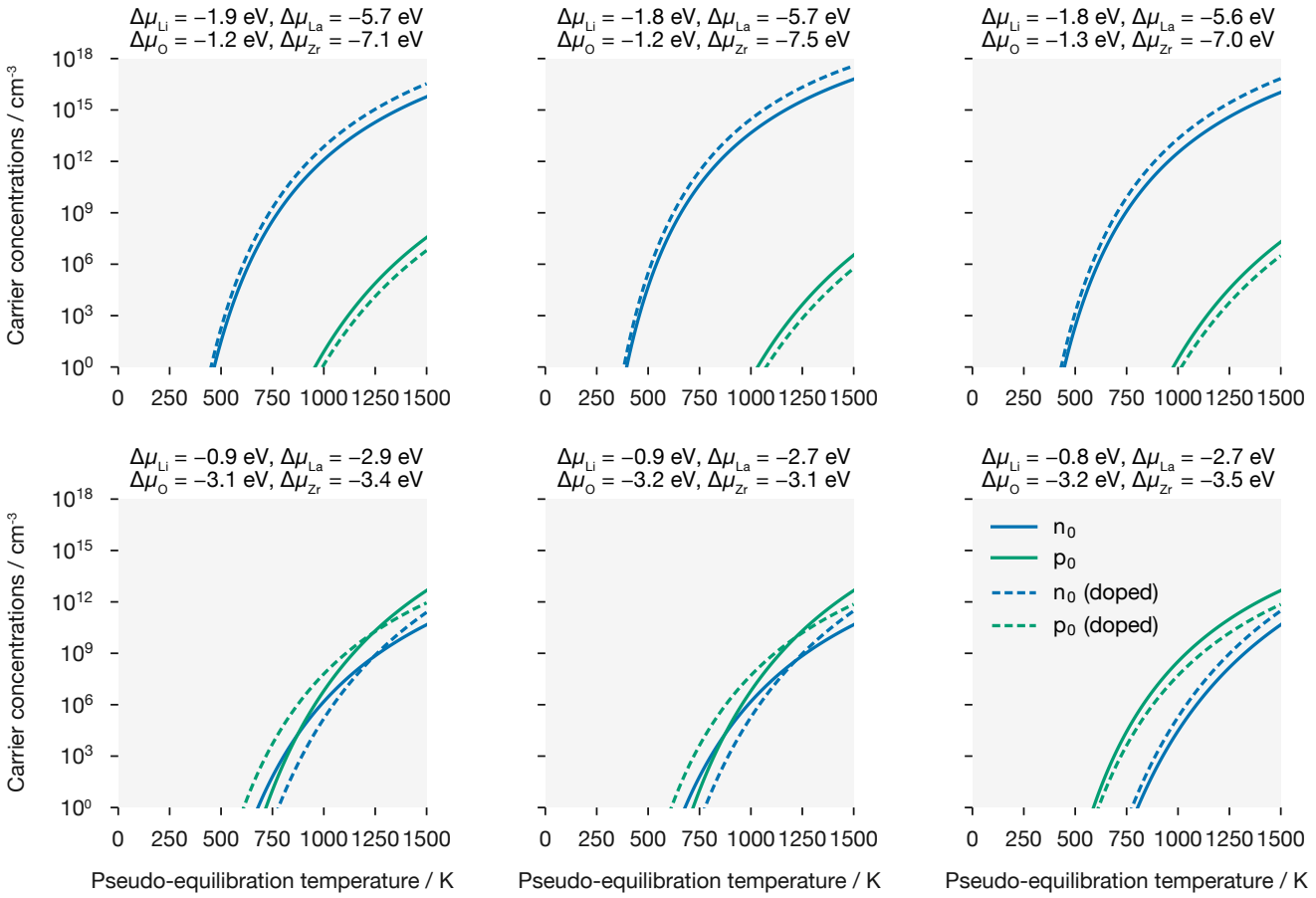

Figure 4: n- and p-type carrier concentrations at six sets of chemical potentials (each set corresponds to a vertex of the estimated chemical potential stability region that LLZO can be synthesised within). The chemical potentials used to calculate defect concentrations are shown above each plot. The grey dotted lines indicate the carrier concentrations that will give rise to electronic conductivities previously proposed at upper bounds on electronic conductivity for dendrite free cycling ($1 \times 10^{-10}\,\mathrm{S\,cm^{-1}}$ and $1 \times 10^{-12}\,\mathrm{S\,cm^{-1}}$).[15] when considering an electron mobility of $0.06\,\mathrm{cm^2\,V^{-1}\,s^{-1}}$. The carrier concentrations are calculated at 1500 K initially, the concentrations of all defects other than lithium vacancies, interstitials and electron and hole concentrations are then fixed to these high temperature values for subsequent, lower temperature solutions. All carrier concentrations are given for both a undoped sample, and a sample containing 0.15 per formula unit of some dopant M^{2+}.

lower temperatures corresponding to typical operating conditions—approximately 298 K. We assume that host-framework point-defects, i.e. those involving La, Zr, or O, formed during synthesis are "frozen in" during subsequent cooling to operating temperatures. The kinetic barriers for the reorganization of such defects within the host-framework are large, which prevents the system from fully re-equilibrating at low temperatures on experimentally relevant timescales[28,52]. Because LLZO is a fast-ion solid electrolyte, with highly-mobile lithium interstitials and vacancies, we do, however, expect V_{Li} and $\mathrm{Li_i}$ defects to re-equilibrate during cooling. Similarly electron and hole populations are expected to re-equilibrate on experimentally-relevant timescales.

To obtain electron and hole carrier concentrations under operating conditions, as a function of initial synthesis conditions, we therefore first calculate self-consistent defect and charge-carrier concentrations for the relevant range of elemental chemical potentials at a characteristic synthesis temperature of 1500 K. We then fix the concentrations of all defects, except for V_{Li} and $\mathrm{Li_i}$, and recompute pseudo-equilibrium defect and charge-carrier populations at a range of lower temperatures, to predict how carrier concentrations change during sample cooling. For this second calculation, we impose the constraint that there is no net lithium exchange with the surroundings during cooling, i.e. the lithium stoichiometry is determined by the high-temperature synthesis conditions.

To illustrate the effect of varying synthesis conditions on the resulting carrier concentrations, we consider six chemical potential "limits", which correspond to the vertices of the synthetically-accessible chemical-potential space. These chemical-potential limits can be grouped into two groups depending on whether they can be broadly characterised as O-rich/metal-poor or

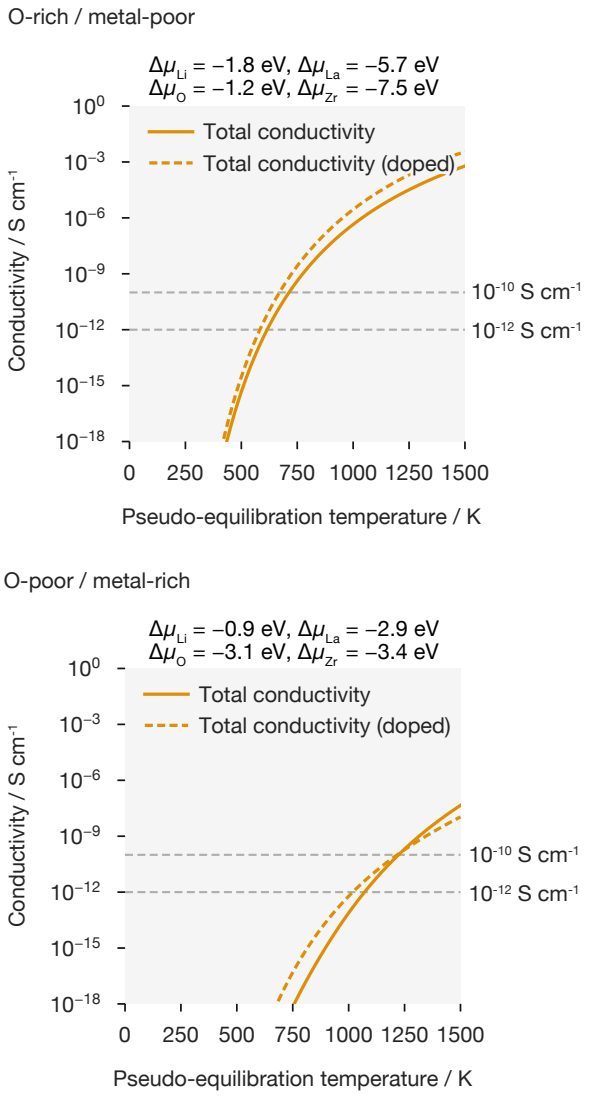

Figure 5: Effective "room temperature" (298 K) electronic conductivities for LLZO synthesised under O-rich/metal-poor (top panel) and O-poor/metal-rich (bottom panel) conditions, as a function of $\{V_{\mathrm{Li}}, \mathrm{Li_i}\}$ and $\{\mathrm{e}^-/\mathrm{h}^\bullet\}$ pseudo-equilibration temperature. Conductivities are calculated via Eqn. 1), using the electronic carrier concentrations in Fig. 4 and the previously calculated maximum room-temperature electron and hole carrier mobilities of $0.06\,\mathrm{cm^2\,V^{-1}\,s^{-1}}$. Solid lines show results for undoped LLZO, and dashed lines show results under supervalent doping with M^{2+} at a concentration of 0.15 per formula unit.

O-poor/metal-rich. Fig. 4 shows the calculated pseudo-equilibrium electron and hole carrier-concentrations as a function of the second re-equilibration temperature, for each of these limits. For each set of synthesis conditions (elemental chemical potentials) we present data for undoped LLZO, where only intrinsic defects are present, and for aliovalently-doped LLZO, where we introduce a concentration of 0.15 per formula unit of a generic supervalent dopant with relative charge $r = +2$—this models the effect of aliovalent dopants, such as a M^{3+} dopant occupying a lithium site, i.e. $M_{\mathrm{Li}}^{\bullet\bullet}$ (see Equation 6).[16,51,53]

Under O-rich/metal-poor conditions (Fig. 4; top panels) we predict strongly n-type behaviour, with the number of free electrons greatly exceeding that of free holes. In contrast, under O-poor/metal-rich conditions (Fig. 4; bottom panels), we predict roughly comparable numbers of electron and hole carriers; with the balance of overall n-type versus p-type behaviour depending on the specific thermodynamic conditions. The total number of charge carriers (summing both electrons and holes) under O-poor/metal-rich conditions, however, is much smaller than under O-rich/metal-poor conditions. The prediction that O-rich/metal-poor conditions give more-strongly n-type samples is initially counter-intuitive; metal oxides typically n-type under O-poor conditions due to the formation of $V_{\mathrm{O}}^{\bullet\bullet}$ donor defects.[26,54] In LLZO, however, the defect chemistry is dominated by cationic defects, such as $\mathrm{Li}_{\mathrm{Zr}}^{\prime\prime\prime}$ acceptor defects, under all but extremely oxygen-deficient conditions.[28]

Electronic Conductivities. Under both O-rich/metal-poor and O-poor/metal-rich conditions, net carrier concentrations are relatively high at the initial synthesis temperature of 1500 K, but decrease by many orders of magnitude as the temperature is reduced under pseudo-equilibrium conditions. The significance of this decrease in carrier concentrations can be seen more clearly if we scale the predicted carrier concentrations by the calculated maximum room-temperature carrier mobility of $0.06\,\mathrm{cm^2\,V^{-1}\,s^{-1}}$ to obtain approximate electronic conductivites (via Eqn. 1). The resulting "room-temperature" intrinsic (undoped) and extrinsic (doped) electronic conductivities are plotted in Fig. 5 for exemplar O-rich/metal-poor and O-poor/metal-rich conditions, as a function of the temperature at which the $\mathrm{e}^-/\mathrm{h}^\bullet$ and $V_{\mathrm{Li}}/\mathrm{Li_i}$ popuations re-equilibrate. In both cases, the high carrier concentrations for as-synthesised samples (1500 K) correspond to room-temperature electronic conductivities well in excess of the threshold values proposed by Han *et al.* For these high bulk electronic conductivities to be observed under operating conditions, however, would require that the electron and hole carrier populations do not re-equilibrate during, or after, sample cooling. Re-equilibration of the electron and hole carrier populations (and the lithium vacancy and interstitial populations), however, greatly reduces the carrier concentrations (Fig. 4) and the corresponding room-temperature ionic conductivites are predicted to be well below the threshold values proposed for bulk

lithium-dendrite growth.

Summary and Discussion

Lithium-dendrite growth in lithium-garnet solid electrolytes is one of the biggest issues preventing their use in solid-state lithium-metal–anode batteries, making a mechanistic understanding of the factors affecting dendrite growth a key research question. One proposed mechanism for dendrite growth in lithium-garnets is the direct reduction of lithium ions to lithium metal within the solid electrolyte bulk, with this facilitated by high residual electronic conductivities.[15,22] Motivated by this proposal, and to provide an estimate of the room-temperature bulk electronic conductivities of lithium-garnet solid electrolytes, we have calculated the electronic conductivity of the lithium-conducting solid electrolyte LLZO from first principles, as a function of synthesis conditions and doping protocol.

We find that electronic carrier have low mobilities ($\leq$0.06 $\mathrm{cm^2\,V^{-1}\,s^{-1}}$) owing to large hole and electron effective masses and strong electron–phonon interactions. While the electronic carrier populations predicted under typical synthesis conditions ($\sim$1500 K) are sufficiently high that the corresponding room-temperature electronic conductivities would be well in excess of the threshold values proposed by Han *et al.*, these electronic carrier populations decrease significantly under subsequent sample cooling. At room-temperature, assuming full re-equilibration of $\mathrm{e^-/h^\bullet}$ carriers (and $V_{\mathrm{Li}}/\mathrm{Li_i}$ defects), carrier concentrations are predicted to be negligible, giving room-temperature electronic conductivities that are well below the threshold values of Han *et al.*. This result is consistent with recent experimental data that gave a much lower electronic conductivity for single-crystal samples of LLZO than previously reported for polycrystalline samples.[55]

Our analysis presented here exclusively considers bulk defect populations and their response to doping, and therefore we cannot exclude the possibility that other sources of free charge-carriers might facilitate direct in-place reduction of lithium ions to lithium metal. Previous theoretical work has observed dramatic band-gap reductions at the surfaces of LLZO ($E_{\mathrm{g}}^{\mathrm{bulk}} = 5.46\,\mathrm{eV}$, $E_{\mathrm{g}}^{\mathrm{surface}} = 2.19\,\mathrm{eV}$).[19] Such band-gap narrowing is expected to greatly increase the number of free charge-carriers at thermal equilibrium, potentially giving high local electronic conductivities. We also note previous experimental observations of lithium nucleation at grain boundaries within LLZO samples,[18] which further highlights the possible critical role of extended defects on dendrite growth and battery failure processes in lithium garnest and other solid lithium-ion electrolytes. While our approach provides a rigorous workflow to assess *bulk* electronic conductivity, future extensions should consider the role of surfaces and extended defects in determining electron concentrations and mobilities.

Computational Methods and Data Access

We have used DFT data taken from our previous study of the intrinsic defect chemistry of tetragonal LLZO[28], which are available as Ref.[56]. Scripts used to generate Figs. 2–5 are available at Ref.[57], and the raw data is available at Ref.[58]. This analysis relies on several open-source Python packages, including Pymatgen[59], matplotlib[60], pandas[61], numpy[62], scipy[63] Phonopy-Spectroscopy[64] vasppy[65,66], tqdm[67], effmass[47], and the Julia package PolaronMobility.jl.[68] The code used to model defect and carrier concentrations is available at Ref.[69] a Python implementation of the Fortran code SC-Fermi.[70]

All DFT data used in this study have been computed using the plane-wave DFT code VASP.[71–73] Interactions between core and valence electrons are described using pseudopotentials within the projector-augmented wave (PAW) method.[74] Unless otherwise noted, all calculations used the hybrid-DFT functional HSE06[75,76] and utilised a plane wave energy cutoff of 520 eV; optimised lattice parameters were obtained by performing a series of constant-volume geometry optimisation calculations, and fitting the resulting energy–volume data to the Murnaghan equation of state.[77] k-point sampling was selected to ensure energies converged to $<$1 meV/atom: all LLZO calculations used a $2\times2\times2$ Monkhorst-Pack k-point mesh. k-point sampling for competing phases and elemental reference calculations is described in the supporting dataset.[58]

The high-frequency dielectric function was calculated using the method of Gajdoš *et al.*,[78] while the ionic response was calculated using Density Functional Perturbation Theory using the PBEsol GGA functional.[79] Effective masses are calculated from fitting to the LLZO band structure, calculated non-selfconsistently using the charge density data computed during a single-point electronic structure calculation following geometry optimisation.

We use the supercell approach for calculating defect formation energies.[39,40] The defects considered in our study are: lithium vacancies and interstitials, V_{Li} and $\mathrm{Li_i}$; oxygen vacancies and interstitials, V_{O} and $\mathrm{O_i}$; holes on framework oxygen $\mathrm{O_O^\bullet}$, lanthanum and zirconium vacancies, V_{La} and V_{Zr}; zirconium interstitials, $\mathrm{Zr_i}$; and cation anti-sites $\mathrm{La_{Zr}}$, $\mathrm{Zr_{Li}^{oct}}$, $\mathrm{Zr_{Li}^{tet}}$, $\mathrm{Zr_{La}}$, $\mathrm{Li_{La}}$, $\mathrm{La_{Li}^{oct}}$ and $\mathrm{Li_{Zr}}$ – a superscript oct or tet denotes a defect located at an octahedral or tetrahedral Li site, respectively. Structural relaxations for all defects were calculated with cell parameters fixed to the optimised values for stoichiometric LLZO. Electrostatic potentials of the bulk and defective calculations were aligned via the difference in spatially averaged electrostatic potentials in the two simulation cells. For this study, we have used the image charge correction scheme of Lany and Zunger,[38] adapted for anisotropic systems by Murphy and Hine.[80]

Acknowledgements

The research was funded by the Royal Society (grant nos. UF100278, UF130329, and URF\R\191006), the Faraday Institution (grant no. FIRG003), EPSRC (grant nos. EP/L01551X/1 and EP/N01572X/1), and the European Research Council, ERC, (grant no. 758345). This work used the Michael computing cluster. Additionally, this work used the ARCHER UK National Supercomputing Service (http://www.archer.ac.uk), with access provided via our membership of the UK's HPC Materials Chemistry Consortium, which is funded by EPSRC grants EP/L000202 and EP/R029431.

References

(1) Lin, D.; Liu, Y.; Cui, Y. *Nature Nanotech.* **2017**, *12*, 194 EP –, Review Article.

(2) Wu, F.; Maier, J.; Yu, Y. *Chem. Soc. Rev.* **2020**, *49*, 1569–1614.

(3) Krauskopf, T.; Richter, F. H.; Zeier, W. G.; Janek, J. *Chem. Rev.* **2020**,

(4) Xu, W.; Wang, J.; Ding, F.; Chen, X.; Nasybulin, E.; Zhang, Y.; Zhang, J.-G. *Energy Environ. Sci.* **2014**, *7*, 513–537.

(5) Monroe, C.; Newman, J. *J. Electrochem. Soc.* **2005**, *152*.

(6) Janek, J.; Zeier, W. G. *Nature Ener.* **2016**, *1*, 1–4.

(7) Zhu, Y.; He, X.; Mo, Y. *ACS Appl. Mater. & Inter.* **2015**, *7*, 23685–23693.

(8) Zhang, Z.; Shao, Y.; Lotsch, B.; Hu, Y.-S.; Li, H.; Janek, J.; Nazar, L. F.; Nan, C.-W.; Maier, J.; Armand, M.; Chen, L. *Energy & Enviro. Sci.* **2018**, *11*, 1945–1976.

(9) Kraft, M. A.; Ohno, S.; Zinkevich, T.; Koerver, R.; Culver, S. P.; Fuchs, T.; Senyshyn, A.; Indris, S.; Morgan, B. J.; Zeier, W. G. *J. Am. Chem. Soc.* **2018**, *140*, 16330–16339.

(10) Famprikis, T.; Canepa, P.; Dawson, J. A.; Islam, M. S.; Masquelier, C. *Nature Mater.* **2019**, *21*, 1–14.

(11) Ohno, S.; Banik, A.; Dewald, G. F.; Kraft, M. A.; Krauskopf, T.; Minafra, N.; Till, P.; Weiss, M.; Zeier, W. G. *Prog. Energy* **2020**, *2*, 022001–36.

(12) Li, Y.; Han, J.-T.; Wang, C.-A.; Xie, H.; Goodenough, J. B. *J. Mater. Chem.* **2012**, *22*, 15357.

(13) Thompson, T.; Yu, S.; Williams, L.; Schmidt, R. D.; Garcia-Mendez, R.; Wolfenstine, J.; Allen, J. L.; Kioupakis, E.; Siegel, D. J.; Sakamoto, J. *ACS Energy Lett.* **2017**, *2*, 462–468.

(14) Flatscher, F.; Philipp, M.; Ganschow, S.; Wilkening, H. M. R.; Rettenwander, D. *J. Mater. Chem. A* **2020**,

(15) Han, F.; Westover, A. S.; Yue, J.; Fan, X.; Wang, F.; Chi, M.; Leonard, D. N.; Dudney, N. J.; Wang, H.; Wang, C. *Nature Ener.* **2019**, *4*, 187–196.

(16) Pesci, F.; Brugge, R. H.; Hekselman, A. K. O.; Cavallaro, A.; Chater, R. J.; Aguadero, A. *J. Mater. Chem. A* **2018**, *6*, 19817–19827.

(17) Cao, D.; Sun, X.; Li, Q.; Natan, A.; Xiang, P.; Zhu, H. *Matter* **2020**, *3*, 57–94.

(18) Song, Y.; Yang, L.; Zhao, W.; Wang, Z.; Zhao, Y.; Wang, Z.; Zhao, Q.; Liu, H.; Pan, F. *Adv. Ener. Mater. 9*, 1900671.

(19) Tian, H.-K.; Liu, Z.; Ji, Y.; Chen, *Chem. Mater.* **2019**, *31*, 7351–7359.

(20) Krauskopf, T.; Dippel, R.; Hartmann, H.; Peppler, K.; Mogwitz, B.; Richter, F. H.; Zeier, W. G.; Janek, J. *Joule* **2019**, *3*, 2030–2049.

(21) Kazyak, E.; Garcia-Mendez, R.; LePage, W. S.; Sharafi, A.; Davis, A. L.; Sanchez, A. J.; Chen, K.-H.; Haslam, C.; Sakamoto, J.; Dasgupta, N. P. *Matter* **2020**, *2*, 1025–1048.

(22) Aguesse, F.; Manalastas, W.; Buannic, L.; Lopez del Amo, J. M.; Singh, G.; Llordés, A.; Kilner, J. *ACS Appl. Mater. & Inter.* **2017**, *9*, 3808–3816.

(23) Jonghe, L. C. D.; Feldman, L.; Buechele, A. *Sol. Stat. Ionics* **1981**, *5*, 267–269, Proceedings of the International Conference on Fast Ionic Transport in Solids.

(24) De Jonghe, L. C.; Feldman, L.; Beuchele, A. *J. Mater. Sci.* **1981**, *16*, 780–786.

(25) Chen, Z.; Li, W.; Li, R.; Zhang, Y.; Xu, G.; Cheng, H. *Langmuir* **2013**, *29*, 13836–13842.

(26) Scanlon, D. O.; Kehoe, A. B.; Watson, G. W.; Jones, M. O.; David, W. I. F.; Payne, D. J.; Egdell, R. G.; Edwards, P. P.; Walsh, A. *Phys. Rev. Lett.* **2011**, *107*.

(27) Scanlon, D. O.; King, P. D. C.; Singh, R. P.; de la Torre, A.; Walker, S. M.; Balakrishnan, G.; Baumberger, F.; Catlow, C. R. A. *Adv. Mater.* **2012**, *24*, 2154–2158.

(28) Squires, A. G.; Scanlon, D. O.; Morgan, B. J. *Chem. Mater.* **2020**, *32*, 1876–1886.

(29) de Walle, C. G. V. *Phys. Rev. Lett.* **2000**, *85*, 1012–1015.

(30) Squires, A. G.; Morgan, B. J. *In preparation* **2020**,

(31) Zhu, Z.; Chu, I.-H.; Deng, Z.; Ong, S. P. *Chem. Mater.* **2015**, *27*, 8318–8325.

(32) Bernstein, N.; Johannes, M. D.; Hoang, K. *Phys. Rev. Lett.* **2012**, *109*.

(33) Fuchs, T.; Culver, S. P.; Till, P.; Zeier, W. G. *ACS Energy Lett.* **2019**, *5*, 146–151.

(34) Kittel, C. *Thermal Physics*; W. H. Freeman: San Francisco, 1980.

(35) Ashcroft, N. *Solid State Physics*; Cengage Learning: Andover England, 1976.

(36) Zhang, S. B.; Northrup, J. E. *Phys. Rev. Lett.* **1991**, *67*, 2339–2342.

(37) Buckeridge, J.; Veal, T. D.; Catlow, C. R. A.; Scanlon, D. O. *Phys. Rev. B* **2019**, *100*.

(38) Lany, S.; Zunger, A. *Phys. Rev. B* **2008**, *78*, 235104.

(39) Kim, S.; Hood, S.; Park, J.; Whalley, L.; Walsh, A. *J. Phys.: Energy* **2020**,

(40) Freysoldt, C.; Grabowski, B.; Hickel, T.; Neugebauer, J.; Kresse, G.; Janotti, A.; Van de Walle, C. G. *Rev. Mod. Phys.* **2014**, *86*, 253–305.

(41) Hellwarth, R. W.; Biaggio, I. *Phys. Rev. B* **1999**, *60*, 299–307.

(42) Feynman, R. P. *Phys. Rev.* **1955**, *97*, 660–665.

(43) Yu, P. Y.; Cardona, M. *Fundamentals of Semiconductors*; Springer Berlin Heidelberg, 2010.

(44) Davies, D. W.; Savory, C. N.; Frost, J. M.; Scanlon, D. O.; Morgan, B. J.; Walsh, A. *J. Phys. Chem. Lett.* **2019**, *11*, 438–444.

(45) Whalley, L. D.; Frost, J. M.; Morgan, B. J.; Walsh, A. *Phys. Rev. B* **2019**, *99*, 085207.

(46) Bradley, C. J. *The Mathematical Theory of Symmetry in Solids: Representation Theory for Point Groups and Space Groups*; Clarendon Press: Oxford New York, 2010.

(47) Whalley, L. D. *J. Open Source Soft.* **2018**, *3*, 797.

(48) Canepa, P.; Dawson, J. A.; Gautam, G. S.; Statham, J. M.; Parker, S. C.; Islam, M. S. *Chem. Mater.* **2018**, *30*, 3019–3027.

(49) CRC Handbook, *CRC Handbook of Chemistry and Physics, 88th Edition*, 88th ed.; CRC Press, 2007.

(50) Finnis, M.; Lozovoi, A.; Alavi, A. *Annu. Rev. Mater. Res.* **2005**, *35*, 167–207.

(51) Thangadurai, V.; Narayanan, S.; Pinzaru, D. *Chem. Soc. Rev.* **2014**, *43*, 4714–4727.

(52) Bachrach, R. Z.; Krusor, B. S. *Journal of Vacuum Science and Technology* **1981**, *18*, 756–764.

(53) Brugge, R.; Kilner, J.; Aguadero, A. *Sol. Stat. Ionics* **2019**, *337*, 154 – 160.

(54) Keating, P. R. L.; Scanlon, D. O.; Morgan, B. J.; Galea, N. M.; Watson, G. W. *J. Phys. Chem. C* **2012**, *116*, 2443–2452.

(55) Philipp, M.; Gadermaier, B.; Posch, P.; Hanzu, I.; Ganschow, S.; Meven, M.; Rettenwander, D.; Redhammer, G. J.; Wilkening, H. M. R. *Adv. Mater. Inter.* **2020**, 2000450.

(56) Squires, A. G.; Scanlon, D. O.; Morgan, B. J. Dataset for Native Defects and their Doping Response in the Lithium Solid Electrolyte $Li_7La_3Zr_2O_{12}$. `https://researchdata.bath.ac.uk/691/`.

(57) `github.com/alexsquires/llzo_elect_conductivty`.

(58) awaiting DOI.

(59) Ong, S. P.; Richards, W. D.; Jain, A.; Hautier, G.; Kocher, M.; Cholia, S.; Gunter, D.; Chevrier, V. L.; Persson, K. A.; Ceder, G. *Comp. Mater. Sci.* **2013**, *68*, 314 – 319.

(60) Hunter, J. D. *Comput. Sci. Eng.* **2007**, *9*, 90–95.

(61) McKinney, W. Data Structures for Statistical Computing in Python. Proceedings of the 9th Python in Science Conference. 2010; pp 51 – 56.

(62) Walt, S. v. d.; Colbert, S. C.; Varoquaux, G. *Comput. Sci. Eng.* **2011**, *13*, 22–30.

(63) Virtanen, P. et al. *Nature Meth.* **2020**, *17*, 261–272.

(64) Skelton, J. M.; Burton, L. A.; Jackson, A. J.; Oba, F.; Parker, S. C.; Walsh, A. *Phys. Chem. Chem. Phys.* **2017**, *19*, 12452–12465.

(65) Morgan, B. J. vasppy. 2019; `https://doi.org/10.5281/zenodo.2667551`.

(66) Morgan, B. J. **2018**, https://github.com/bjmorgan/vasppy.

(67) da Costa-Luis, C. O. *J. Open Source Soft.* **2019**, *4*, 1277.

(68) Frost, J. M. *Physical Review B* **2017**, *96*.

(69) `https://github.com/bjmorgan/py-sc-fermi`.

(70) Buckeridge, J. *Comp. Phys. Commun.* **2019**, *244*, 329–342.

(71) Kresse, G.; Hafner, J. *Phys. Rev. B* **1993**, *47*, 558–561.

(72) Kresse, G.; Hafner, J. *Phys. Rev. B* **1994**, *49*, 14251–14269.

(73) Kresse, G.; Furthmüller, J. *Phys. Rev. B* **1996**, *54*, 11169–11186.

(74) Blöchl, P. E. *Phys. Rev. B* **1994**, *50*, 17953–17979.

(75) Heyd, J.; Scuseria, G. E.; Ernzerhof, M. *J. Chem. Phys.* **2003**, *118*, 8207–8215.

(76) Krukau, A. V.; Vydrov, O. A.; Izmaylov, A. F.; Scuseria, G. E. *J. Chem. Phys.* **2006**, *125*.

(77) Murnaghan, F. D. *Proc. Nat. Acad. Sci.* **1944**, *30*, 244–247.

(78) Gajdoš, M.; Hummer, K.; Kresse, G.; Furthmüller, J.; Bechstedt, F. *Phys. Rev. B* **2006**, *73*, 045112.

(79) Perdew, J. P.; Ruzsinszky, A.; Csonka, G. I.; Vydrov, O. A.; Scuseria, G. E.; Constantin, L. A.; Zhou, X.; Burke, K. *Phys. Rev. Lett.* **2008**, *100*.

(80) Murphy, S. T.; Hine, N. D. M. *Phys. Rev. B* **2013**, *87*, 094111.